Proximity-effect engineering in aluminum-based planar Josephson junctions with intrinsic superconductivity

K.B. Polevoy,[1,2] S.V. Bakurskiy,[3,1] V.I. Ruzhickiy,[1,3,2] S.V. Egorov,[4] A.G. Shishkin,[2,1] A.S. Frolov,[2,5] M.A. Kirsanova,[6,7] I.N. Krupatin,[7] A.V. Yanilkin,[2,1] N.V. Klenov,[8,9] I.I. Soloviev,[3,1] A.A. Golubov,[2,10] M.Yu. Kupriyanov,[2,3] and V.S. Stolyarov[2,1,*]

[1] *All-Russian Research Institute of Automatics n.a. N.L. Dukhov (VNIIA), Moscow 127030, Russia*
[2] *Moscow Institute of Physics and Technology, Dolgoprudny 141700, Russia*
[3] *Skobeltsyn Institute of Nuclear Physics, Lomonosov Moscow State University, Moscow 119991, Russia*
[4] *Institute of Solid State Physics RAS, 2 Academician Osipyan str., Chernogolovka, Moscow Oblast 142432, Russia*
[5] *Lomonosov Moscow State University, Leninskie Gory 1/3, Moscow 119991, Russia*
[6] *Center for Energy Science and Technology, Skolkovo Institute of Science and Technology, Bolshoy Boulevard, 30, bld. 1, Moscow 121205, Russia*
[7] *Advanced Imaging Core Facility, Skolkovo Institute of Science and Technology, Bolshoy Boulevard, 30, bld. 1, Moscow 121205, Russia*
[8] *Faculty of Physics, Lomonosov Moscow State University, Moscow 119992, Russia*
[9] *Moscow Technical University of Communications and Informatics (MTUCI), Moscow 111024, Russia*
[10] *HSE University, Moscow 101000, Russia*

(Received 6 August 2025; revised 15 December 2025; accepted 23 December 2025; published 10 February 2026)

We present a comprehensive study of planar Nb-Al-Nb Josephson junctions with submicrometer dimensions ($L \approx 100$ nm, active area of approximately 5×10^4 nm^2), where the intrinsic superconductivity of the aluminum weak link plays a crucial role in enhancing device performance. Through a combination of theoretical modeling and experimental characterization, we demonstrate that the aluminum interlayer significantly boosts the critical current $I_c \approx 50$ μA and the characteristic voltage $V_c \approx 1$ mV at $T = 4$ K, while maintaining the nonhysteretic current-voltage characteristics essential for digital applications. Our microscopic model, based on self-consistent solutions of the Usadel equations, reveals that this enhancement originates from the coexistence of proximity-induced superconductivity and intrinsic pairing in aluminum, which is particularly pronounced at an optimal boundary resistance. Structural analysis confirms epitaxial Nb-Al interfaces with minimal interdiffusion, enabling reproducible fabrication of these compact junctions. These results establish Nb-Al-Nb bridges as promising building blocks for high-density superconducting electronics operating at helium temperatures.

DOI: 10.1103/s1k7-wvw2

I. INTRODUCTION

The development of superconducting electronics is crucial for advancing energy-efficient computing systems [1–5], quantum computer interfaces [6–9], and neuromorphic circuits [10–13]. A key challenge in this field is the miniaturization of superconducting circuits. Conventional single-flux quantum (SFQ) logic circuits currently achieve an integration density of approximately 10^6–10^7 Josephson junctions per cm^2 [14], which remains significantly lower than the approximately 1.3×10^{10} transistors per cm^2 typical of complementary metal-oxide-semiconductor technology. The scalability of the superconductor-insulator-superconductor (SIS) Josephson junctions traditionally used in SFQ circuits is severely limited, requiring areas of the order of 1 μm^2 due to low critical current density and the need for additional shunting [5,15,16]. Attempts to increase the current density and reduce the junction area lead to significant inhomogeneity and a large parameter spread, which can prevent the use of these junctions in large-scale integrated circuits.

While high-critical-temperature (high-T_c) superconductors, such as $YBa_2Cu_3O_{7-x}$ and MgB_2, offer advantages like higher operating temperatures and current densities, their integration into large-scale digital circuits faces fundamental challenges. A key issue in materials such as $YBa_2Cu_3O_{7-x}$ is the *d*-wave symmetry of the order parameter [17]. This phenomenon causes intrinsic spatial inhomogeneity of the Josephson current density at grain boundaries and bicrystal interfaces, and in ion-irradiated weak links. Although extensive work has been conducted studying high-T_c junctions and their applications in digital circuits [18–48], the intrinsic spatial inhomogeneities at interfaces lead to poor reproducibility and significant

*Contact author: stolyarov.vs@phystech.edu

parameter spread in fabricated junctions. Planar junctions formed in NbN [49–51] and in MgB_2 [52,53] also face similar problems. It should also be noted that Josephson contacts fabricated with a focused ion beam face limitations on their width. The requirement for reproducible parameters restricts their size to the micrometer scale. This limitation stems from the significant difference in transport properties between the weak-link regions at the edges and in the middle of the structure [26]. Collectively, these material-specific limitations make high-T_c junctions less suitable for high-density, reproducible superconducting circuits than the mature niobium-based technology.

The International Roadmap for Devices and Systems Outbriefs [5] considers planar superconductor–normal-metal–superconductor (SNS) Josephson bridges, consisting of superconducting (S) electrodes separated by a normal-metal (N) region, as a promising solution for miniaturization [5,16,54]. These junctions are typically realized using either nanowires [55–65] or finite-length normal-metal segments with superconducting electrodes [Fig. 1(a)]. Such planar bridges enable the reduction of the weak-link region to 100–200 nm while maintaining high critical currents I_c and large characteristic voltages $V_c = I_c R_n$.

Despite these advantages, material selection remains a critical challenge. While niobium (Nb) is the established standard for superconducting electrodes, the choice of normal-metal weak-link materials is less straightforward. Common candidates include thin films of copper (Cu) [66–80], gold (Au) [81–83], silver (Ag) [84], and aluminum (Al) [85–89]. In particular, in Ref. [89], it was shown that in the NbN-Al junctions, the critical current density at 300 mK can be 30% higher than that of Al nanowires with the same lateral dimensions as the NbN-based devices. These findings demonstrate the importance of using superconducting barriers in hybrid nanodevices. The achievement of a very high Josephson current in the NbN/Al junctions is of great relevance for superconducting circuits requiring a high integration density.

The transport properties of SN-N-NS junctions depend not only on the interelectrode distance L but also on the interface transparency and the overlap between the S and N films [16,90,91]. The transparency of Nb-Al interfaces in particular has been extensively studied [92–100]. These interfaces can exhibit tunnel-like behavior even without intentional oxide layers, depending on the deposition conditions [99–107]. Unfortunately, the application of multilayer Nb-Al-Nb sandwiches is limited by their asymmetry, which arises from differences between the Nb-Al and Al-Nb boundaries. The planar NbAl-Al-AlNb geometry [Figs. 1(a) and 1(b)] of the junctions solves this problem because both Al-Nb boundaries are manufactured using the same technological process. Moreover, existing inhomogeneities in the interface are averaged by the large coherence length ξ in the aluminum layer.

The electronic properties of such junctions are usually considered in two temperature regimes: (i) for temperatures T above the critical temperature of Al (T_c^*), they are interpreted as conventional SN-N-NS junctions; (ii) at $T \ll T_c^*$, they may function as SIS′-S′-S′IS junctions [89] (as two superconducting tunnel junctions connected in series).

In this work, we demonstrate that Al's intrinsic superconductivity plays a crucial role over the whole temperature range and amplifies the proximity effect, even for $T > T_c^*$. Therefore, aluminum serves as an exceptional weak-link material for superconducting nanoelectronics, outperforming traditional normal metals such as Cu, Au, or Ag. We fabricate NbAl-Al-AlNb bridges with $L \approx 100$ nm and an active area of approximately 5×10^4 nm^2, achieving $V_c \approx 1$ mV, $I_c \approx 50$ μA, and $R_n \approx 20\ \Omega$ at $T \approx 4$ K. These results are supported by a microscopic theoretical model and comprehensive structural and transport measurements, highlighting the potential of Al-based junctions for next-generation superconducting circuits.

II. THEORY OF S-S′-S BRIDGES

For the theoretical analysis of the studied structures, we employ an extended version of the SN-N-NS junction model [16], which accounts for the intrinsic superconductivity of the Al material with critical temperature $T_c^* < T_c$, where T_c is the critical temperature of the Nb electrodes. We assume the dirty-limit conditions for both the Al and Nb layers, with the Al-layer thickness d_{Al} being much smaller than the coherence length $\xi_{\mathrm{Al}} = (D_{\mathrm{Al}}/2\pi T_c)^{1/2}$, where D_{Al} is the diffusion coefficient of aluminum. Additionally, we neglect the suppression of superconductivity in the Nb electrodes due to the inverse proximity effect with the Al layer.

Under these conditions, the problem can be reduced [16, 90,108] to the one-dimensional Usadel equations [109] in an Al strip [see Eqs. (A1)–(A10)] for details]. In the central region ($|x| \le L/2$), the equation takes the form

$$\frac{1}{\omega G}\frac{\partial}{\partial x}\left(G^2\frac{\partial\Phi}{\partial x}\right) = \Phi - \Delta, \tag{1}$$

while under the Nb electrodes ($L/2 \le |x| \le L_{I1,I2} + L/2$), we have

$$\frac{1}{\omega G}\frac{\partial}{\partial x}\left(G^2\frac{\partial\Phi}{\partial x}\right) = \frac{\Phi - \delta e^{i\varphi\,\mathrm{sgn}(x)/2}}{\xi_{\mathrm{eff}}^2} - \Delta. \tag{2}$$

The self-consistency equation in the N layer is given by

$$\Delta \ln\frac{T}{T_c^*} + \frac{T}{T_c}\sum_{\omega=-\infty}^{\infty}\left(\frac{\Delta}{|\omega|} - \frac{\Phi G}{\omega}\right) = 0. \tag{3}$$

Here, the anomalous Usadel Green's function Φ corresponds to the pairing amplitude in the Al strip, while

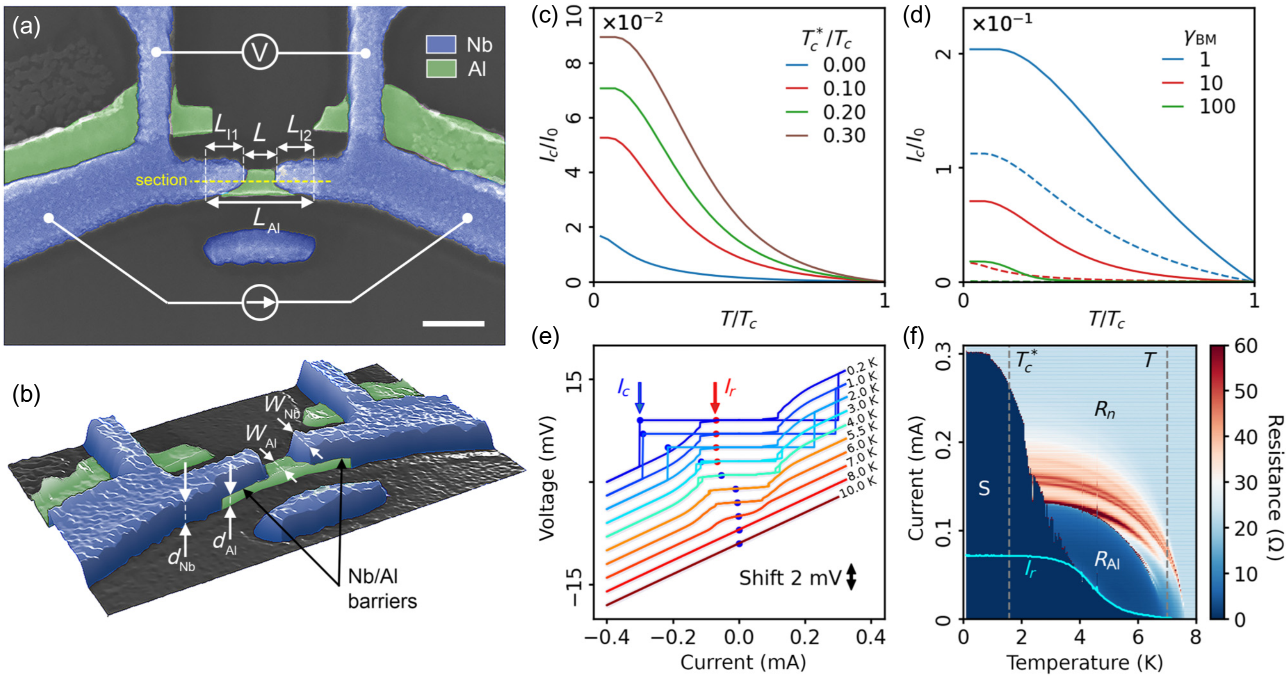

FIG. 1. Geometry of Josephson junctions and temperature-dependent electron-transport properties. (a) Typical false-colored scanning electron microscope image of the studied Nb-Al-Nb structures. Green corresponds to the Al film, blue to the Nb film. White lines connecting electrodes indicate the standard four-probe measurement scheme. Characteristic dimensions are marked by white arrows and symbols: L, distance between Nb leads; L_{Al}, length of the Al nanobridge; L_{I1} and L_{I2}, lengths of the Nb-Al overlap regions at the left and right interfaces, respectively. The yellow line indicates the area examined by transmission electron microscope (TEM) (results shown in Fig. 3). Scale bar: 200 nm. (b) 2.5D schematic of the Nb-Al-Nb structure. Definitions: d_{Nb} and d_{Al}, thicknesses of the Nb and Al layers, respectively; W_{Al}, width of the Al nanobridge; W_{Nb}, width of Nb leads. (c),(d) Theoretical temperature dependence of the critical current I_c for SN-N-NS Josephson junctions with $L = 2\xi_{\mathrm{Al}}$ for (c) $\gamma_{\mathrm{BM}} = 10$ with varying critical temperature T_c^* of the N-film and (d) $T_c^* = 0.2T_c$ (solid line) and $T_c^* = 0$ (dashed line) with different suppression parameters $\gamma_{\mathrm{BM}} = 1, 10, 100$. (e) Current-voltage characteristics at temperatures from 0.2 to 10 K. Curves are vertically offset for clarity. Blue circles mark the critical current I_c, red circles mark the retrapping current I_r. (f) Differential resistance colormap as a function of increasing current at different temperatures. Color scale indicates differential resistance values. The dark blue region (marked "S") represents the superconducting state. The cyan line tracks the retrapping current I_r during current decrease. Above 4 K, I_c and I_r coincide. R_n indicates the normal-state resistance, T_c is the Nb critical temperature, and T_c^* is the Al critical temperature.

the normal Green's function $G = \omega/(\omega^2 + \Phi_\omega \Phi^*_{-\omega})^{1/2}$ describes the amplitude of the probability density of the electron to be unpaired; $\omega = (2n+1)T/T_c$ represents the Matsubara frequencies. The effective coherence length in Al under the Nb electrode is $\xi^2_{\mathrm{eff}} = \gamma_{\mathrm{BM}}\omega/(G_{\mathrm{Nb}} + \gamma_{\mathrm{BM}}\omega)$, the proximity-induced pairing potential $\delta = G_{\mathrm{Nb}}\Delta_{\mathrm{Nb}}/(G_{\mathrm{Nb}} + \gamma_{\mathrm{BM}}\omega)$. Further, φ denotes the phase difference between the S electrodes. The values Δ_{Nb} and G_{Nb} are the pair potential and normal Green's functions in the Nb electrode, while Δ is the pair potential in the Al strip. The parameters with dimensions of energy, Φ, Δ, Δ_{Nb}, and ω, are normalized to πT_c. The bridge boundary $\gamma_{\mathrm{BM}} = \gamma_B d_{\mathrm{Al}}/\xi_{\mathrm{Al}}$ incorporates the boundary-suppression parameter [110] $\gamma_B = R_b/\rho_{\mathrm{Al}}\xi_{\mathrm{Al}}$, where R_b is the specific boundary resistance of the SN interface and ρ_{Al} and ξ_{Al} are the aluminum resistivity and coherence length, respectively. The coordinate x is normalized to ξ_{Al} and measured from the structure's center.

Notably, Eq. (2) reduces to Eq. (1) for a completely opaque interface ($\gamma_{\mathrm{BM}} \to \infty$).

The current $I(x)$ through the Al strip is given by

$$\frac{I(x)}{I_0} = \frac{T}{T_c} \sum_{\omega=-\infty}^{\infty} \frac{G^2}{\omega^2} \left(\mathrm{Im}\,\Phi \frac{\partial\, \mathrm{Re}\,\Phi}{\partial x} - \mathrm{Re}\,\Phi \frac{\partial \mathrm{Im}\,\Phi}{\partial x} \right), \tag{4}$$

where the normalized current $I_0 = J_0 W d$, the characteristic current density $J_0 = \pi T_c/e\xi_{\mathrm{Al}}\rho_{\mathrm{Al}}$, and W is the width of the structure.

We solved the boundary-value problem [Eqs. (1) and (2)] numerically using the boundary conditions $d\Phi/dx = 0$ at $x = \pm L_{\mathrm{Al}}/2 = \pm(L/2 + L_I)$. Figure 1(c) shows the calculated temperature dependence of the critical current $I_c(T)$ for $L = 2\xi_{\mathrm{Al}}$, $L_I = 3\xi_{\mathrm{Al}}$, $\gamma_{\mathrm{BM}} = 10$, and various T_c^* values ranging from 0 to $0.3T_c$. Increasing T_c^* from 0 to $0.1T_c$ enhances $I_c(0)$ by a factor of 3, while the intrinsic superconductivity in the Al layer extends the low-temperature plateau in $I_c(T)$.

Figure 1(d) presents $I_c(T)$ curves for $L = 2\xi_{\mathrm{Al}}$, $L_I = 3\xi_{\mathrm{Al}}$, and $\gamma_{\mathrm{BM}} = 1$, 10, and 100, comparing cases with $T_c^* = 0$ (dashed lines) and $T_c^* = 0.2T_c$ (solid lines). The relative I_c enhancement due to Al's intrinsic superconductivity becomes more pronounced at larger γ_B values, where the electrode proximity effect is suppressed by boundary opacity. These γ_{BM}-dependent features arise from two distinct sources of superconducting correlations in the Al layer at $T \lesssim T_c^*$: (i) intrinsic superconductivity (parameter Δ) and (ii) electrode-induced correlations (parameter δ). For highly transparent boundaries ($\gamma_{\mathrm{BM}} \lesssim 1$), the $I_c(T)$ dependence shows no discontinuity at $T = T_c^*$, with only an overall I_c increase [Fig. 1(d), $\gamma_{\mathrm{BM}} = 1$]. Conversely, for opaque boundaries ($\gamma_{\mathrm{BM}} \gtrsim 1$), $I_c(T)$ exhibits a sharp increase at $T = T_c^*$ followed by strong high-temperature suppression.

Our fabricated NbAl-Al-AlNb bridges (Fig. 1) correspond to the intermediate case with $\gamma_{\mathrm{BM}} \approx 10$, which is a typical value of the interface parameter for planar Josephson SNS bridges [63,83].

III. FABRICATION AND CHARACTERIZATION OF NbAl-Al-AlNb BRIDGES

NbAl-Al-AlNb junctions were fabricated using a shadow deposition technique. A two-layer mask prepared by electron-beam lithography enabled the sequential deposition of a 32-nm aluminum layer at 16° to the substrate normal, followed by a 91-nm niobium layer along the normal direction, both deposited via electron-beam evaporation in a single vacuum cycle with residual pressure 3×10^{-8} mbar ensuring no contamination or Al oxidation [111] at the interface.

This process yielded a series of Josephson junctions exhibiting critical currents of approximately 50 μA at 4 K. Table I summarizes their geometric parameters and transport properties at 4 K, with samples ordered by interelectrode distance L.

Figures 1(e) and 1(f) present the transport characteristics of a representative nanostructure (sample P in Table I). Figure 1(e) shows the current-voltage characteristics from 0.2 to 10 K, while Fig. 1(f) displays the differential resistance dV/dI as a function of current and temperature.

The critical current emerges at $T_c \approx 7$ K, corresponding to the critical temperature of the Nb-Al overlap region. A resistance jump at 7.6 K [Fig. 1(d)] marks the Nb electrodes' critical temperature. Between 7 and 4 K, the I-V curves show no hysteresis, with I_c increasing to 50 μA at 4 K. The differential resistance $R(I) = dV/dI$ rises smoothly from $R_{\mathrm{Al}} \approx 3.5\ \Omega$ ($I \gtrsim I_c$) to $R_{\mathrm{Al}}^* \approx 6\ \Omega$ ($I \approx 100$ μA).

At $I \approx 100$ μA, one NbAl boundary transitions to the resistive state, evidenced by a sharp $R(I)$ increase.

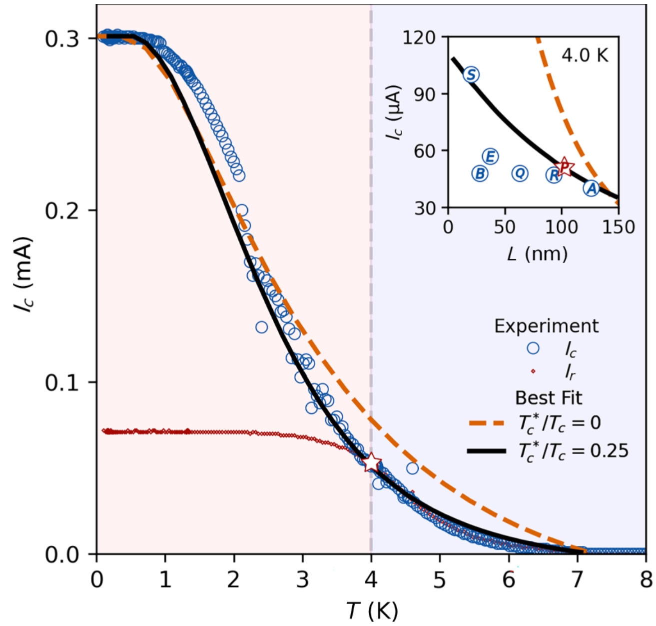

FIG. 2. Temperature dependence of critical currents. Critical current I_c (blue circles) and retrapping current I_r (red dots) of sample P as functions of temperature T. The black solid and orange dashed lines show the best fits to the $I_c(T)$ dependence with and without accounting for intrinsic Al superconductivity, respectively. Inset: critical current I_c versus interelectrode distance L at $T = 4$ K for samples listed in Table I, along with model $I_c(L)$ dependencies calculated using parameters obtained from fitting the main panel data (sample P, red star).

Further current increases sequentially drive the second NbAl boundary, NbAl electrode regions, and adjacent Nb films into the resistive state. Ultimately, $R(I)$ reaches approximately 23 Ω, matching the normal-state resistance above T_c. Notably, the Nb-Al boundary transition current differs from equilibrium Nb-Al tunnel junctions due to nonequilibrium electron energy distributions in the Al layer.

Below 4 K, characteristic SNS junction hysteresis appears in the I-V curves [Fig. 1(e)], caused by electron-gas overheating during resistive-to-superconducting transitions. At $T \lesssim 1$ K, $I_c \approx 300$ μA exceeds the retrapping current $I_r \approx 75$ μA by a factor of 4. The return branch shows sequential superconducting transitions: NbAl boundaries at 120 μA and the Al layer at 75 μA. The low-temperature characteristic voltage reaches approximately 7 mV.

Figure 2 shows the temperature-dependent I_c for sample P, exhibiting the characteristic SNS junction behavior: exponential decay at high T and a low-T plateau [74,91]; however, our junctions show an unusually broad plateau and higher crossover temperatures compared to Au- or Cu-based SNS bridges [61–63]. Conventional SN-N-NS fitting without Al superconductivity ($T_c^* = 0$) yields $\xi_{\mathrm{Al}} = 41$ nm, $\rho_{\mathrm{Al}} = 4.5$ μΩcm, $\gamma_{\mathrm{BM}} = 1.1$, and $T_c = 7.2$ K (orange dashed line).

TABLE I. Geometric parameters [see Figs. 1(a) and 1(b)] and transport properties at $T = 4$ K of Nb-Al-Nb junctions [see Figs. 1(e) and 1(f)]. Here, L, $L_{\rm Al}$, $W_{\rm Al}$, $W_{\rm Nb}$, $L_{\rm I1}$, and $L_{\rm I2}$ were determined based on a scanning electron microscope image similar to Fig. 1(a). The values of $d_{\rm Al}$ and $d_{\rm Nb}$ are based on the TEM image in Fig. 3(a).

Sample	L (nm)	$L_{\rm Al}$ (nm)	$W_{\rm Al}$ (nm)	$W_{\rm Nb}$ (nm)	$L_{\rm I1}$ (nm)	$L_{\rm I2}$ (nm)	$d_{\rm Al}$ (nm)	$d_{\rm Nb}$ (nm)	R_n (Ω)	I_c (μA)	$V_c^{\rm Al}$ (mV)	V_c (mV)
S	20	361	70	185	178	148	32	91	18	100	0.30	1.80
B	28	441	61	198	215	206	32	91	16	48	0.05	0.77
E	37	237	63	179	116	82	32	91	23	57	0.50	1.15
Q	63	356	87	163	159	150	32	91	22.6	48	0.15	1.08
R	93	241	65	167	87	81	32	91	23.9	47	0.24	1.12
P	**102**	**442**	**107**	**144**	**177**	**153**	**32**	**91**	**22.9**	**51**	**0.17**	**1.17**
A	126	412	88	121	153	149	32	91	20	40	0.16	0.80

Taking into account intrinsic Al superconductivity in the frame of the modified SS′-S′-S′S model (black solid line) improves the fit with $T_c^* = 1.8$ K, $\xi_{\rm Al} = 49$ nm, $\rho_{\rm Al} = 3.3$ μΩcm, and $\gamma_{\rm BM} = 10.3$. In this case, the estimates of material parameters become closer to the literature thin-film values [112,113], the interface parameter $\gamma_{\rm BM}$ is comparable to typical SNS bridge values [63,83], and T_c^* is within the interval 1.25–2.7 K of experimentally estimated values of the critical temperature of thin Al films in multilayered structures [15,98,114–116]. It should be noted that the aluminum parameters T_c^* and $\rho_{\rm Al}$ are sensitive to reduction of the electron mean free path or structural deformations [117,118], and they may be significantly different in isolated thin films and multilayer devices.

It is important to clarify that we do not claim a higher I_cR_n product for our SNS junctions compared to conventional Nb-Al-AlO$_x$-Nb SIS junctions. The key advantage of our Nb-Al-Nb bridges lies in their high critical current density ($J_c \sim 10^5$ A/cm^2), which enables a drastic reduction of the junction area (to approximately 5×10^4 nm^2) while maintaining nonhysteretic operation at 4 K, without the need for external shunting. This is a fundamental step toward miniaturization, whereas SIS junctions are limited by their lower J_c (typically 1–10 kA/cm^2) and require shunting to eliminate hysteresis, complicating scaling.

The inset of Fig. 2 shows the distribution of critical currents I_c for samples with different distances between the electrodes, $L = 20$–120 nm. For comparison, we also show the possible $I_c(L)$ dependencies calculated using the best-fit parameters obtained above for sample P from the $I_c(T)$ dependence within the SN-N-NS (dashed orange line) and SS′-S′-S′S (black solid line) models. Although a direct comparison of these dependencies with the experimental points is not valid due to the spread of geometrical parameters in the other bridges, the general trend of the black line is close to the obtained results. At the same time, predictions made by the SN-N-NS model for shorter junctions fail and exceed the measured critical currents by several orders of magnitude.

Thus, we found that the standard SN-N-NS model cannot be used to describe Nb-Al-Nb contacts even at temperatures T significantly exceeding the critical temperature of aluminum T_c^*. For an accurate description of the electronic structure and the current properties of the Josephson junction, it is necessary to account for the effect of proximity amplification due to the intrinsic superconductivity of aluminum and to use the modified SS′-S′-S′S model. In SS′IS′S tunnel structures, a similar enhancement of the critical current was discussed in Ref. [98] (see Fig. 8 of this reference).

Regarding the nature of the junction, we note that the normal-state resistance R_n (20–23 Ω) is significantly larger than the resistance of the Al bridge alone (approximately 3.5–6 Ω). This indicates that the interface resistances dominate, a signature of an SNS structure with low-transparency barriers. The temperature dependence of R_n in our measurement range ($T \leq 10$ K) is governed by residual resistance (impurity and defect scattering) and does not show the strong metallic increase associated with phonon scattering, which is typical for this low-temperature regime.

A cross-sectional transmission electron microscope (TEM) analysis [Fig. 3(a)] reveals distinct 32-nm Al and 91-nm Nb layers with minimal intermixing, as confirmed by TEM energy-dispersive x-ray spectroscopy measurements. The Al layer exhibits a characteristic polycrystalline structure with grain sizes ranging from 30 to 90 nm [Fig. 3(b)], typical for electron-beam-evaporated films [113,119], while the Nb layer shows significantly smaller grains of 10–15 nm that maintain epitaxial alignment with the substrate [Fig. 3(c)]. The interface region displays partial lattice disorder, suggesting imperfect atomic registry between the two materials [120] [Fig. 3(c), inset]. Complementary molecular-dynamics simulations performed using a $46 \times 55 \times 56$-nm^3 simulation cell (3.5×10^6 atoms) at 600 K [used to accelerate the simulation time (18 ns) compared to the experimental timescale] reproduce key experimental observations, including Nb grain sizes of 5–20 nm and the Nishiyama-Wasserman orientation relationship between the Al and Nb lattices: $(111)_{\rm Al} \parallel (110)_{\rm Nb}$, $[1\bar{1}0]_{\rm Al} \parallel [001]_{\rm Nb}$ [121,122] [Fig. 3(d)]. The simulations reveal that the interface-formation mechanism involves substitution of Al surface atoms by deposited Nb atoms rather than conventional interdiffusion, attributable to Nb's

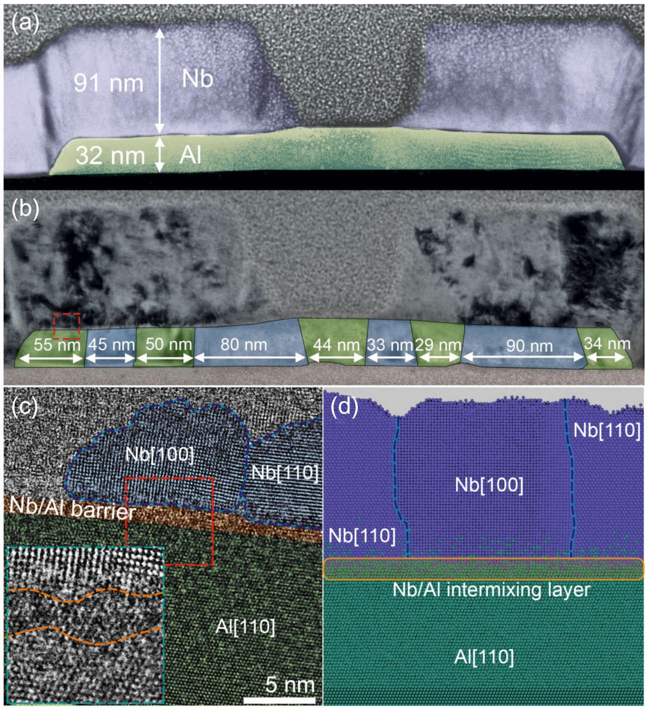

FIG. 3. Cross-sectional analysis of the Nb-Al interface. (a) Scanning electron microscope image of the junction cross section, showing the complete aluminum layer (32 nm) and niobium layer (91 nm). (b) Dark-field TEM image of the same region as in (a), revealing individual Al grains with their respective sizes. Red dashed squares indicate the area magnified in (c). (c) High-resolution view of the Al-Nb interface. The lower green region represents part of a single Al monocrystalline grain. The upper Nb layer shows two distinct grains (approximately 10 nm in size), highlighted in blue color. Scale bar: 5 nm. Red dashed squares indicate the area magnified in the inset. Inset: enlarged view of Nb-Al interface. (d) Results of molecular-dynamics simulation of Nb deposition on an Al single crystal.

significantly higher cohesive energy (7.57 eV/atom versus 3.39 eV/atom for Al) and surface tension (2.10 J/m^2 versus 1.14 J/m^2 for Al). This substitutional process creates a metastable Nb-Al intermixing layer that can subsequently relax into the more thermodynamically stable $NbAl_3$ intermetallic phase given sufficient time under typical deposition conditions.

IV. DISCUSSION

Our investigation of NbAl-Al-AlNb bridges with variable thickness demonstrates that electron-beam deposition technology can produce structures with atomically sharp interfaces between nearly single-crystal Al submicrometer blocks and columnar-structured Nb films. Figure 3(c) reveals spatial variations in the transport properties of the NbAl boundary, showing both amorphous regions separating single-crystal Nb and Al blocks, and epitaxially connected Nb-Al regions.

In conventional three-layer NbAlNb sandwiches [102–107], the NbAl and AlNb interfaces exhibit significantly different morphologies. While NbAl boundaries typically show relatively uniform transparency similar to NbAl-AlO_x-Nb tunnel junctions [99–101], the AlNb interfaces resemble those observed in our work. The presence of even one interface with the morphology shown in Fig. 3(c) inevitably creates substantial inhomogeneity in the critical current density, leading to poor parameter reproducibility in NbAlNb sandwiches. Such junctions [102–107] typically behave as asymmetric SNIS or SS′IS devices.

The solution lies in restoring symmetry through transition to double-barrier SINIS or SIS′IS structures [15]. In Nb-I-Al-I-Nb junctions, the probability of forming both highly transparent epitaxial Nb-I-Al and Al-I-Nb interfaces is negligible. Moreover, aluminum's coherence length exceeds typical Nb crystalline block dimensions, enabling averaging of superconducting correlations within the Al layer.

Unlike previous studies [102–107], our planar Nb-Al-Nb bridges feature NbAl and AlNb interfaces fabricated in a single deposition cycle with comparable transport properties. The critical current in these bridges is determined by the anomalous Green's function amplitudes at the Al film boundaries with the NbAl and AlNb electrodes, representing the averaged superconducting correlations (both intrinsic and induced) within the Al sublayer. The significant size difference between Nb crystallites (approximately 10–15 nm) and Al's coherence length (approximately 50 nm) enables self-averaging of interface inhomogeneities, making boundary effects less pronounced than in sandwich-type Nb-I-Al-I-Nb junctions.

For a direct comparison with the widely used Nb-Al-AlO_x-Nb SIS junctions, we note that while SIS junctions offer superior reproducibility and uniformity, our Nb-Al-Nb bridges provide a path to much higher integration density due to their smaller area (approximately 0.05 μm^2 vs approximately 1 μm^2 for SIS) and intrinsic nonhysteretic behavior at 4 K without external shunting. The I_cR_n product of our junctions (around 1 mV) is comparable to that of typical SIS junctions used in SFQ circuits. The key trade-off is between miniaturization or scalability (favored by our bridges) and mature process uniformity (favored by SIS).

V. CONCLUSION

Our experimental studies demonstrate that NbAl-Al-AlNb Josephson junctions exhibit several key advantages for superconducting nanoelectronics applications. The fabricated devices show: (i) compact dimensions ($L_{Al} \times W \approx 5 \times 10^4$ nm^2), significantly smaller than conventional tunnel junctions; (ii) hysteresis-free current-voltage characteristics at operating temperatures

($T \gtrsim 4$ K), eliminating the need for external shunting; and (iii) excellent electrical parameters at 4 K, including a critical current $I_c \approx 50$ μA, a normal-state resistance $R_n \approx 20\ \Omega$, and a characteristic voltage V_c comparable to tunnel-junction performance.

The device with these parameters outperforms planar junctions using alternative weak-link materials. These unique properties occur due to the intrinsic superconductivity of the Al film, which significantly amplifies the proximity effect, even above the aluminum critical temperature T_c^*. It is likely that the mutual Nb-Al proximity-effect amplification will also allow the electrode dimensions to be reduced to the hundred-nanometer scale without a reduction in their effective critical temperature, in contrast to the behavior recently observed in Nb-Au-Nb junctions [83].

These results conclusively validate the proposed approach [16] of using variable-thickness bridges with Nb superconducting electrodes and an Al-based weak link for compact active elements in superconducting circuits. The interfaces exhibit tunnel-like conductivity with a suppression parameter $\gamma_{\mathrm{BM}} \approx 10$ while maintaining excellent device performance. Crucially, our electron-beam deposition technique enables the fabrication of structures with atomically sharp interfaces between layers, providing a pathway for further miniaturization of superconducting elements without compromising their performance characteristics.

ACKNOWLEDGMENTS

The design and fabrication of the samples were carried out with the financial support of the Russian Science Foundation (Project No. 25-19-00057, https://rscf.ru/project/25-19-00057/). We thank the Russian Science Foundation (Grant No. 23-72-00020) for supporting the TEM investigations of Nb-Al-Nb nanobridges. Measurements and theoretical description of the Josephson junctions were supported by the Ministry of Science and Higher Education of the Russian Federation (Agreement No. 075-15-2025-010).

DATA AVAILABILITY

The data that support the findings of this article are not publicly available upon publication because it is not technically feasible and/or the cost of preparing, depositing, and hosting the data would be prohibitive within the terms of this research project. The data are available from the authors upon reasonable request.

APPENDIX A: Φ PARAMETRIZATION

In this study, we analyze NbAl-Al-AlNb bridges while disregarding the processes that take place within the Nb layers. For the S′ material (aluminum, which has intrinsic superconductivity), the Usadel equation [109] in the Φ parametrization is given by

$$\xi_{\mathrm{Al}}^2 \frac{\partial}{\partial x}\left(G^2 \frac{\partial \Phi}{\partial x}\right) + \xi_{\mathrm{Al}}^2 \frac{\partial}{\partial y}\left(G^2 \frac{\partial \Phi}{\partial y}\right) - \frac{\omega G \Phi}{\pi T_c} = -\frac{\omega G \Delta_{\mathrm{Al}}}{\pi T_c}. \tag{A1}$$

In this expression, the anomalous Usadel Green's functions F are related to the functions $\Phi = \Phi_\omega$ by the expression $F = \Phi_\omega/(\omega^2 + \Phi_\omega \Phi_{-\omega}^*)^{1/2}$ and represent the pairing amplitude in the Al strip, whereas the normal Green's function $G = G_\omega = \omega/(\omega^2 + \Phi_\omega \Phi_{-\omega}^*)^{1/2}$ describes the probability amplitude of an electron remaining unpaired. The parameter $\xi_{\mathrm{Al}} = (D_{\mathrm{Al}}/2\pi T_c)^{1/2}$ is the coherence length of aluminum, T_c is the critical temperature of niobium, D_{Al} is the Al diffusion coefficient, and Δ_{Al} is the pair potential in the Al strip. Here, $\omega = (2n+1)\pi T$ are the Matsubara frequencies, and the x and y axes are directed along and perpendicular to the SN interfaces, respectively.

Equation (A1) should be solved with the Kupriyanov-Lukichev [110] conditions at SN interfaces,

$$\gamma_B \xi_{\mathrm{Al}} G \frac{\partial}{\partial y}\frac{\Phi}{\omega} = G_{\mathrm{Nb}}\left(\frac{\Phi_s}{\omega} - \frac{\Phi}{\omega}\right) \tag{A2}$$

and

$$\frac{\partial}{\partial n}\Phi = 0, \tag{A3}$$

where n is a unit vector in the direction perpendicular to a free interface. The term $G_{\mathrm{Nb}} = (\omega/\sqrt{\omega^2 + \Delta_{\mathrm{Nb}}^2})$ in Eq. (A2) represents the normal Green's function in the Nb electrode, while Φ_s is given by

$$\Phi_s = \Delta_{\mathrm{Nb}} e^{i\phi}. \tag{A4}$$

Here, Δ_{Nb} is the superconducting order parameter in the bulk S electrode and $\phi = \varphi\,\mathrm{sgn}(x)/2$ denotes the phase of the order parameter at the SN interfaces. The boundary-suppression parameter [110] $\gamma_B = R_b/\rho_{\mathrm{Al}}\xi_{\mathrm{Al}}$, where R_b is the specific boundary resistance of the SN interface and ρ_{Al} and ξ_{Al} are the aluminum resistivity and coherence length, respectively.

In the limit of small Al layer thickness d_{Al} compared to ξ_{Al}, the functions Φ (A1) depend only weakly on the coordinate y. Performing integration over the y coordinate and taking into account the boundary conditions (A2) and (A3), we arrive at the following one-dimensional equation for the function $\Phi(x)$ at each frequency ω:

$$\frac{\pi T_c \xi_{\mathrm{Al}}^2}{\omega G}\frac{\partial}{\partial x}\left(G^2 \frac{\partial \Phi}{\partial x}\right) + \frac{\pi T_c G_s(\Delta_{\mathrm{Nb}} e^{i\phi} - \Phi)}{\omega \gamma_{\mathrm{BM}}} + \Delta_{\mathrm{Al}} = \Phi, \tag{A5}$$

where $\gamma_{\mathrm{BM}} = \gamma_B d_{\mathrm{Al}}/\xi_{\mathrm{Al}}$.

For convenience, we rewrite the equation in a normalized form by introducing the following parameters: the effective coherence length in Al under the Nb electrode $\xi_{\text{eff}}^2 = \gamma_{\text{BM}}\omega/(G_{\text{Nb}} + \gamma_{\text{BM}}\omega)$ and the proximity-induced pairing potential $\delta = G_{\text{Nb}}\Delta_{\text{Nb}}/(G_{\text{Nb}} + \gamma_{\text{BM}}\omega)$. All energy-related parameters (Φ, Δ, Δ_{Nb}, and the Matsubara frequencies ω) are normalized to πT_c. Finally, the coordinate x is normalized to ξ_{Al} and is measured from the structure's center. Using the introduced notation, we can rewrite Eq. (A5) in the form convenient for our purposes, as in (1):

$$\frac{1}{\omega G}\frac{\partial}{\partial x}\left(G^2\frac{\partial \Phi}{\partial x}\right) = \frac{\Phi - \delta e^{i\varphi\,\text{sgn}(x)/2}}{\xi_{\text{eff}}^2} - \Delta_{\text{Al}}. \tag{A6}$$

In the area of the Al strip not covered by the electrode, the parameters simplify to $\xi_{\text{eff}}^2 = 1$ and $\delta = 0$.

The superconducting order parameters Δ_{Nb} and Δ_{Al} are determined by the following self-consistency equations:

$$\Delta_{\text{Nb}} \ln\frac{T}{T_c} + \pi T \sum_{\omega=-\infty}^{\infty}\left(\frac{\Delta_{\text{Nb}}}{|\omega|} - \frac{\Delta_{\text{Nb}}}{\sqrt{\omega^2 + \Delta_{\text{Nb}}^2}}\right) = 0, \tag{A7}$$

$$\Delta_{\text{Al}} \ln\frac{T}{T_c^*} + \pi T \sum_{\omega=-\infty}^{\infty}\left(\frac{\Delta_{\text{Al}}}{|\omega|} - \frac{\Phi G}{\omega}\right) = 0. \tag{A8}$$

Following normalization by πT_c, these equations transform into Eq. (3) in the main text:

$$\Delta_{\text{Nb}} \ln\frac{T}{T_c} + \frac{T}{T_c} \sum_{\omega=-\infty}^{\infty}\left(\frac{\Delta_{\text{Nb}}}{|\omega|} - \frac{\Delta_{\text{Nb}}}{\sqrt{\omega^2 + \Delta_{\text{Nb}}^2}}\right) = 0, \tag{A9}$$

$$\Delta_{\text{Al}} \ln\frac{T}{T_c^*} + \frac{T}{T_c} \sum_{\omega=-\infty}^{\infty}\left(\frac{\Delta_{\text{Al}}}{|\omega|} - \frac{\Phi G}{\omega}\right) = 0. \tag{A10}$$

APPENDIX B: FITTING PROCEDURE

The parameters of the model were fitted to the experimental data using the trust-region-reflective algorithm, which is a subspace trust-region method based on the interior-reflective Newton method [123,124]. In this method, each iteration involves the approximate solution of a large linear system via preconditioned conjugate gradients.

Based on a preliminary analysis showing that the $I_c(T)$ dependence is insensitive to the L_I/ξ_{Al} ratio, this parameter was fixed at $L_I/\xi_{\text{Al}} = 6$ for computational convenience. The set of free parameters in the fit included the interelectrode distance L/ξ_m, the boundary parameter γ_{BM}, and the critical temperatures T_c and T_c^*.

Since the experimental data for $I_c(T)$ saturate at low temperatures, we normalized the experimental curve using this saturation value prior to fitting. The theoretical curve was treated in an identical manner.

The theoretical $I_c(T)$ dependence was calculated through a nested loop structure. The outermost loop runs through the desired temperature range (normalized by T_c). For each temperature, the maximum supercurrent I_c is found by searching for the optimal phase difference φ via a bisection method. The current for any given phase φ is itself the result of a complex iterative process. First, a self-consistent solution for the pair potential in aluminum, $\Delta_{\text{Al}}(x)$, must be found. This is achieved by an iterative loop that starts with the initial guess $\Delta_{\text{Al}}(x) = \Delta_{\text{Nb}}$ and converges when the relative update to Δ_{Al} is sufficiently small. Inside this loop, the core calculation involves solving the nonlinear boundary-value problem from Eqs. (1) and (2) by integrating over the Matsubara frequencies until the current profile $I(x)$, given by Eq. (4), converges. The updated Δ_{Al} is then found from its self-consistency equation, Eq. (3).

The mean-squared error between the normalized theoretical and experimental curves served as the cost function for the fitting algorithm. To ensure that a global minimum was found, the fitting procedure was relaunched with different initial guesses for the parameters if the resulting fit was deemed inadequate. Finally, after obtaining the best-fit parameters, the scaling factor I_0 was determined by comparing the absolute values of the saturation currents from theory and experiment at low temperatures.

[1] O. A. Mukhanov, Energy-efficient single flux quantum technology, IEEE Trans. Appl. Supercond. **21**, 760 (2011).

[2] S. K. Tolpygo, Superconductor digital electronics: Scalability and energy efficiency issues, Low Temp. Phys. **42**, 361 (2016).

[3] I. I. Soloviev, N. V. Klenov, S. V. Bakurskiy, M. Y. Kupriyanov, A. L. Gudkov, and A. S. Sidorenko, Beyond Moore's technologies: Operation principles of a superconductor alternative, Beilstein J. Nanotechnol. **8**, 2689 (2017).

[4] S. K. Tolpygo, V. Bolkhovsky, R. Rastogi, S. Zarr, A. L. Day, E. Golden, T. J. Weir, A. Wynn, and L. M. Johnson, Advanced fabrication processes for superconductor electronics: Current status and new developments, IEEE Trans. Appl. Supercond. **29**, 1 (2019).

[5] D. S. Holmes, in *2021 IEEE International Roadmap for Devices and Systems Outbriefs* (IEEE, Santa Clara, CA, USA, 2021), pp. 1–93.

[6] A. Opremcak, I. V. Pechenezhskiy, C. Howington, B. G. Christensen, M. A. Beck, E. Leonard, Jr., J. Suttle, C.

Wilen, K. N. Nesterov, G. J. Ribeill *et al.*, Measurement of a superconducting qubit with a microwave photon counter, Science **361**, 1239 (2018).

[7] M. Ahmad, C. Giagkoulovits, S. Danilin, M. Weides, and H. Heidari, Scalable cryoelectronics for superconducting qubit control and readout, Adv. Intell. Syst. **4**, 2200079 (2022).

[8] V. Vozhakov, M. Bastrakova, N. Klenov, A. Satanin, and I. Soloviev, Speeding up qubit control with bipolar single-flux-quantum pulse sequences, Quantum Sci. Technol. **8**, 035024 (2023).

[9] H. Shen, Y. He, Z. Han, Z. Li, W. Luo, L. Cheng, Y. Luo, B. Jing, and N. Yoshikawa, Generating microwave signals with enhancive amplitudes using superconductor single flux quantum pulses for controlling quantum bit, Adv. Quantum Technol. **7**, 240001 (2024).

[10] M. Schneider, E. Toomey, G. Rowlands, J. Shainline, P. Tschirhart, and K. Segall, SuperMind: A survey of the potential of superconducting electronics for neuromorphic computing, Supercond. Sci. Technol. **35**, 053001 (2022).

[11] O. V. Skryabina, A. E. Schegolev, N. V. Klenov, S. V. Bakurskiy, A. G. Shishkin, S. V. Sotnichuk, K. S. Napolskii, I. A. Nazhestkin, I. I. Soloviev, M. Yu. Kupriyanov *et al.*, Superconducting bio-inspired Au-nanowire-based neurons, Nanomaterials **12**, 1671 (2022).

[12] M. A. Jardine and C. J. Fourie, Hybrid RSFQ-QFP superconducting neuron, IEEE Trans. Appl. Supercond. **33**, 1 (2023).

[13] M. A. Karamuftuoglu, A. Bozbey, and S. Razmkhah, JJ-Soma: Toward a spiking neuromorphic processor architecture, IEEE Trans. Appl. Supercond. **33**, 1 (2023).

[14] V. K. Semenov, Y. A. Polyakov, and S. K. Tolpygo, Very large scale integration of Josephson-junction-based superconductor random access memories, IEEE Trans. Appl. Supercond. **29**, 1 (2019).

[15] M. Yu. Kupriyanov, A. Brinkman, A. A. Golubov, M. Siegel, and H. Rogalla, Double-barrier Josephson structures as the novel elements for superconducting large-scale integrated circuits, Physica C **326–327**, 16 (1999).

[16] I. I. Soloviev, S. V. Bakurskiy, V. I. Ruzhickiy, N. V. Klenov, M. Y. Kupriyanov, A. A. Golubov, O. V. Skryabina, and V. S. Stolyarov, Miniaturization of Josephson junctions for digital superconducting circuits, Phys. Rev. Appl. **16**, 044060 (2021).

[17] H. Hilgenkamp and J. Mannhart, Grain boundaries in high-T_c superconductors, Rev. Mod. Phys. **74**, 485 (2002).

[18] S. Tolpygo, B. Nadgorny, S. Shokhor, F. Tafuri, Y. Lin, A. Bourdillon, and M. Gurvitch, Electron beam writing in fabricating planar high-T_c Josephson junctions, Physica C **209**, 211 (1993).

[19] A. J. Pauza, W. E. Booij, K. Herrmann, D. F. Moore, M. G. Blamire, D. A. Rudman, and L. R. Vale, Electron-beam damaged high-temperature superconductor Josephson junctions, J. Appl. Phys. **82**, 5612 (1997).

[20] W. Booij, A. Pauza, D. Moore, E. Tarte, and M. Blamire, in *IEEE Transactions on Applied Superconductivity* (IEEE, Pittsburgh, PA, USA, 1996), Vol. 7, pp. 3025–3028, https://ieeexplore.ieee.org/xpl/tocresult.jsp?isnumber=13488&punumber=77.

[21] K. Chen, S. Cybart, and R. Dynes, Planar thin film $YBa_2Cu_3O_{7-\delta}$ Josephson junction pairs and arrays via nanolithography and ion damage, Appl. Phys. Lett. **85**, 2863 (2004).

[22] N. Bergeal, X. Grison, J. Lesueur, G. Faini, M. Aprili, and J. Contour, High-quality planar high-T_c Josephson junctions, Appl. Phys. Lett. **87**, 102502 (2005).

[23] S. A. Cybart, E. Y. Cho, T. J. Wong, B. H. Wehlin, M. K. Ma, C. Huynh, and R. C. Dynes, Nano Josephson superconducting tunnel junctions in $YBa_2Cu_3O_{7-\delta}$ directly patterned with a focused helium ion beam, Nat. Nanotechnol. **10**, 598 (2015).

[24] E. Cho, M. Ma, C. Huynh, K. Pratt, D. Paulson, V. Glyantsev, R. Dynes, and S. Cybart, $YBa_2Cu_3O_{7-\delta}$ superconducting quantum interference devices with metallic to insulating barriers written with a focused helium ion beam, Appl. Phys. Lett. **106**, 252601 (2015).

[25] B. Müller, M. Karrer, F. Limberger, M. Becker, B. Schröppel, C. J. Burkhardt, R. Kleiner, E. Goldobin, and D. Koelle, Josephson junctions and SQUIDs created by focused helium-ion-beam irradiation of $YBa_2Cu_3O_7$, Phys. Rev. Appl. **11**, 044082 (2019).

[26] C. Schmid, C. Buckreus, D. Haas, M. Pröpper, R. Hutt, C. Magén, D. Hanisch, M. Karrer, M. Schilling, D. Koelle *et al.*, $YBa_2Cu_3O_7$ nano-constriction Josephson junctions and SQUIDs fabricated by focused helium-ion-beam irradiation, arXiv:2511.19197.

[27] A. A. Golubov and M. Yu. Kupriyanov, Anomalous proximity effect in *d*-wave superconductors, JETP Lett. **67**, 501 (1998).

[28] T. Satoh, M. Y. Kupriyanov, J. S. Tsai, M. Hidaka, and H. Tsuge, Resonant-tunneling transport in YBaCuO/PrBa CuO/YBaCuO edge type Josephson-junctions, IEEE Trans. Appl. Supercond. **5**, 2612 (1995).

[29] I. Devyatov and M. Y. Kupriyanov, Resonant tunneling and long-range proximity effect, JETP Lett. **59**, 200 (1994).

[30] A. A. Golubov, M. A. J. Verhoeven, I. A. Devyatov, M. Yu. Kupriyanov, G. J. Gerritsma, and H. Rogalla, Resonant tunneling in $Y(Dy)Ba_2Cu_3O_{7-\delta}/PrBa_2Cu_{3-x}Ga_xO_{7-\delta}/Y(Dy)Ba_2Cu_3O_{7-\delta}$ ramp-type Josephson junctions, Physica C **235–240**, 3261 (1994).

[31] J. Yoshida and T. Nagano, Tunneling and hopping conduction via localized states in thin $PrBa_2Cu_3O_{7-x}$ barriers, Phys. Rev. B **55**, 11860 (1997).

[32] Z. G. Ivanov, V. K. Kaplunenko, E. A. Stepantsov, E. Wikborg, and T. Claeson, An experimental implementation of high-T_c-based RSFQ set-reset trigger at 4.2 K, Supercond. Sci. Technol. **7**, 239 (1994).

[33] B. Oelze, B. Ruck, M. Roth, R. Dömel, M. Siegel, A. Y. Kidiyarova-Shevchenko, T. Filippov, M. Y. Kupriyanov, G. Hildebrandt, H. Töpfer *et al.*, Rapid single-flux-quantum balanced comparator based on high-T_c bicrystal Josephson junctions, Appl. Phys. Lett. **68**, 2732 (1996).

[34] Y. H. Kim, J. H. Kang, J. M. Lee, T. S. Hahn, S. S. Choi, and S. J. Park, Operation of high-T_c SFQ devices at near liquid nitrogen temperature, Physica C **280**, 304 (1997).

[35] B. Oelze, B. Ruck, E. Sodtke, A. Kirichenko, M. Y. Kupriyanov, and W. Prusseit, A 3 bit single flux quantum shift register based on high-T_c bicrystal Josephson

junctions operating at 50 K, Appl. Phys. Lett. **70**, 658 (1997).

[36] B. Ruck, Y. Chong, R. Dittmann, A. Engelhardt, E. Sodtke, and M. Siegel, A high-temperature superconducting delta-sigma modulator based on a multilayer technology with bicrystal Josephson junctions, Supercond. Sci. Technol. **12**, 701 (1999).

[37] Y. H. Kim, J. H. Kang, G. Y. Sung, J. H. Park, J. M. Lee, K. R. Jung, C. H. Kim, T. S. Hahn, and S. S. Choi, Digital and analog measurements of HTS SFQ RS flip-flops and shift register circuits, IEEE Trans. Appl. Supercond. **9**, 3817 (1999).

[38] H. Hasegawa, Y. Tarutani, T. Fukazawa, and K. Takagi, Fabrication of QFP devices from $Au/SrTiO_3YBa_2/Cu_3O_7$ structures, IEEE Trans. Appl. Supercond. **9**, 4087 (1999).

[39] K. Saitoh, Y. Soutome, T. Fukazawa, Y. Tarutani, and K. Takagi, Voltage divider operation using high-T_c superconducting interface-engineered Josephson junctions, Appl. Phys. Lett. **76**, 2606 (2000).

[40] J. D. McCambridge, M. G. Forrester, D. L. Miller, B. D. Hunt, J. X. Pryzbysz, J. Talvacchio, and R. M. Young, Multilayer HTS SFQ analog-to-digital converters, IEEE Trans. Appl. Supercond. **7**, 3622 (1997).

[41] A. H. Sonnenberg, G. J. Gerritsma, and H. Rogalla, Balanced comparator fabricated in ramp edge technology, Physica C **326–327**, 12 (1999).

[42] J. H. Park, J. H. Kim, G. Y. Sung, C. H. Kim, K. R. Jung, J. H. Kang, and T. S. Hahn, Fabrication of RS flip-flops using Y-Ba-Cu-O ramp-edge junctions and their operation, IEEE Trans. Appl. Supercond. **11**, 932 (2001).

[43] Y. Soutome, T. Fukazawa, A. Tsukamoto, K. Saitoh, and K. Takagi, Fabrication of HTS ramp-edge junctions with surface-modified barriers and a ground plane, Physica C **372–376**, 143 (2002).

[44] H. Wakana, S. Adachi, Y. Tarutani, K. Tsubone, K. Nakayama, and K. Tanabe, Improvement of critical current density uniformity for interface-modified Josephson junctions in single flux quantum circuits, Jpn. J. Appl. Phys. **45**, L105 (2006).

[45] M. Maruyama, H. Wakana, T. Hato, H. Suzuki, K. Tanabe, K. Uekusa, T. Konno, N. Sato, and M. Kawabata, HTS sampler with improved circuit design and layout, IEICE Trans. Electron. **E90-C**, 579 (2007).

[46] B. Ruck, B. Oelze, and E. Sodtke, A ring circuit for the determination of dynamic error rates in high-temperature superconductor RSFQ circuits, Supercond. Sci. Technol. **10**, 991 (1997).

[47] B. Ruck, B. Oelze, R. Dittmann, A. Engelhardt, E. Sodtke, W. Booij, and M. Blamire, Measurement of the dynamic error rate of a high temperature superconductor rapid single flux quantum comparator, Appl. Phys. Lett. **72**, 2328 (1998).

[48] K. Saitoh, T. Utagawa, and Y. Enomoto, Temperature dependence of a high-T_c single-flux-quantum logic gate up to 50 K, Appl. Phys. Lett. **72**, 2754 (1998).

[49] J.-Y. Juang, D. A. Rudman, J. Talvacchio, and R. B. van Dover, Effects of ion irradiation on the normal state and superconducting properties of NbN thin films, Phys. Rev. B **38**, 2354 (1988).

[50] W. Xu, Y. Chen, C. Cai, P. Zhu, F. Fan, Z. Liu, Q. Hu, W. Lu, T. Zhang, J. Li *et al.*, Restriction of vortex motion in superconducting NbN film via ion irradiation, Eur. Phys. J. Plus **138**, 1010 (2023).

[51] S. K. Tolpygo, R. Rastogi, D. Kim, T. J. Weir, N. Parmar, and E. B. Golden, Fabrication and properties of NbN/NbN_x/NbN and Nb/NbN_x/Nb Josephson junctions, arXiv:2512.01826.

[52] D. Cunnane, K. Chen, and X. Xi, Superconducting MgB_2 rapid single flux quantum toggle flip flop circuit, Appl. Phys. Lett. **102**, 222601 (2013).

[53] D. Yin, X. Cai, T. Xu, R. Sun, Z. Chen, Y. Han, L. Tian, Y. Wang, Y. Zhang, and Z. Gan, MgB_2 Josephson junctions fabricated by focused helium ion beam with different irradiation doses on SiC and MgO substrates, Physica C **623**, 1354532 (2024).

[54] N. Gusarov, R. Mandal, I. Salameh, I. Holzman, S. Kvatinsky, and Y. Ivry, Low-power rapid planar superconducting logic devices, arXiv:2405.18309.

[55] T. Hoss, C. Strunk, T. Nussbaumer, R. Huber, U. Staufer, and C. Schönenberger, Multiple Andreev reflection and giant excess noise in diffusive superconductor/normal-metal/superconductor junctions, Phys. Rev. B **62**, 4079 (2000).

[56] M. Jung, H. Noh, Y.-J. Doh, W. Song, Y. Chong, M.-S. Choi, Y. Yoo, K. Seo, N. Kim, B.-C. Woo, B. Kim, and J. Kim, Superconducting junction of a single-crystalline Au nanowire for an ideal Josephson device, ACS Nano **5**, 2271 (2011).

[57] W. Gu, H. Choi, and K. K. Kim, Universal approach to accurate resistivity measurement for a single nanowire: Theory and application, Appl. Phys. Lett. **89**, 253102 (2006).

[58] J. Wang, C. Shi, M. Tian, Q. Zhang, N. Kumar, J. K. Jain, T. E. Mallouk, and M. H. W. Chan, Proximity-induced superconductivity in nanowires: Minigap state and differential magnetoresistance oscillations, Phys. Rev. Lett. **102**, 247003 (2009).

[59] M. Kompaniiets, O. V. Dobrovolskiy, C. Neetzel, E. Begun, F. Porrati, W. Ensinger, and M. Huth, Proximity-induced superconductivity in crystalline Cu and Co nanowires and nanogranular Co structures, J. Appl. Phys. **116**, 073906 (2014).

[60] W.-H. Xu, L. Wang, Z. Guo, X. Chen, J. Liu, and X.-J. Huang, Copper nanowires as nanoscale interconnects: Their stability, electrical transport, and mechanical properties, ACS Nano **9**, 241 (2015).

[61] O. Skryabina, S. V. Egorov, A. S. Goncharova, A. Klimenko, S. N. Kozlov, V. V. Ryazanov, S. V. Bakurskiy, M. Y. Kupriyanov, A. A. Golubov, K. S. Napolskii, and V. S. Stolyarov, Josephson coupling across a long single-crystalline Cu nanowire, Appl. Phys. Lett. **110**, 222605 (2017).

[62] O. V. Skryabina, S. V. Bakurskiy, A. G. Shishkin, A. A. Klimenko, K. S. Napolskii, N. V. Klenov, I. I. Soloviev, V. V. Ryazanov, A. A. Golubov, D. Roditchev, M. Yu. Kupriyanov, and V. S. Stolyarov, Environment-induced overheating phenomena in Au-nanowire based Josephson junctions, Sci. Rep. **11**, 15274 (2021).

[63] S. V. Sotnichuk, O. V. Skryabina, A. G. Shishkin, S. V. Bakurskiy, M. Yu. Kupriyanov, V. S. Stolyarov, and K. S. Napolskii, Long single Au nanowires in Nb/Au/Nb Josephson junctions: Implications for superconducting microelectronics, ACS Appl. Nano Mater. **5**, 17059 (2022).

[64] J. Wang, Z. Wang, and P. Wang, Magnetic field enhanced critical current and subharmonic structures in dissipative superconducting gold nanowires, Quantum Front. **1**, 21 (2022).

[65] S. V. Sotnichuk, O. V. Skryabina, S. E. Kushnir, D. N. Khmelenin, S. V. Bakurskiy, V. S. Stolyarov, and K. S. Napolskii, Automated manufacturing of segmented nanowires with thin ferromagnetic layers: A step towards miniature SFS Josephson junctions, J. Mater. Chem. C **13**, 4236 (2025).

[66] J. Warlaumont and R. Buhrman, Planar SNS microbridges, IEEE Trans. Magn. **15**, 570 (1979).

[67] R. B. van Dover, A. de Lozanne, and M. R. Beasley, Superconductor-normal-superconductor microbridges: Fabrication, electrical behavior, and modeling, J. Appl. Phys. **52**, 7327 (1981).

[68] O. Liengme, P. Lerch, W. Liu, and P. Martinoli, Fabrication and electromagnetic properties of planar variable-thickness S-N-S microbridges, IEEE Trans. Magn. **19**, 995 (1983).

[69] J. Sauvageau, R. Ono, A. Jain, K. Li, and J. Lukens, Length dependent properties of SNS microbridges, IEEE Trans. Magn. **21**, 854 (1985).

[70] H. Nakano and T. Aomine, Magnetic field dependence of critical currents in SNS bridges fabricated by direction of sputtering deposition and anodic oxidization, Jpn. J. Appl. Phys. **26**, 304 (1987).

[71] H. Nakano and T. Aomine, Nb-Cu-Nb bridges fabricated by direction of sputtering deposition and anodic oxidization, Jpn. J. Appl. Phys. **25**, L601 (1986).

[72] H. Nakano and T. Aomine, Fabrication procedure of SNS bridges by shapes of sputtering deposition at step edge and anodic oxidization, Shinku **30**, 188 (1987).

[73] F. Ichikawa, T. Fukami, and T. Aomine, Current-voltage characteristics of a triangular loop containing three SNS bridges, Physica C **221**, 195 (1994).

[74] P. Dubos, H. Courtois, B. Pannetier, F. K. Wilhelm, A. D. Zaikin, and G. Schön, Josephson critical current in a long mesoscopic S-N-S junction, Phys. Rev. B **63**, 064502 (2001).

[75] A. Savin, J. P. Pekola, J. Flyktman, A. Anthore, and F. Giazotto, Cold electron Josephson transistor, Appl. Phys. Lett. **84**, 4179 (2004).

[76] H. Courtois, M. Meschke, J. T. Peltonen, and J. P. Pekola, Origin of hysteresis in a proximity Josephson junction, Phys. Rev. Lett. **101**, 067002 (2008).

[77] C. P. García and F. Giazotto, Josephson current in nanofabricated V/Cu/V mesoscopic junctions, Appl. Phys. Lett. **94**, 132508 (2009).

[78] F. Giazotto, J. T. Peltonen, M. Meschke, and J. P. Pekola, Superconducting quantum interference proximity transistor, Nat. Phys. **6**, 254 (2010).

[79] T. E. Golikova, F. Hübler, D. Beckmann, N. V. Klenov, S. V. Bakurskiy, M. Yu. Kupriyanov, I. E. Batov, and V. V. Ryazanov, Critical current in planar SNS Josephson junctions, JETP Lett. **96**, 668 (2013).

[80] T. E. Golikova, M. J. Wolf, D. Beckmann, I. E. Batov, I. V. Bobkova, A. M. Bobkov, and V. V. Ryazanov, Nonlocal supercurrent in mesoscopic multiterminal SNS Josephson junction in the low-temperature limit, Phys. Rev. B **89**, 104507 (2014).

[81] A. Morpurgo, T. Klapwijk, and B. Van Wees, Hot electron tunable supercurrent, Appl. Phys. Lett. **72**, 966 (1998).

[82] L. Angers, F. Chiodi, G. Montambaux, M. Ferrier, S. Guéron, H. Bouchiat, and J. C. Cuevas, Proximity dc squids in the long-junction limit, Phys. Rev. B **77**, 165408 (2008).

[83] O. V. Skryabina, S. V. Bakurskiy, V. I. Ruzhickiy, A. Shishkin, N. V. Klenov, I. I. Soloviev, M. Yu. Kupriyanov, and V. S. Stolyarov, Anomalous influence of electrode width on the critical current of Nb/Au Josephson junctions, Supercond. Sci. Technol. **37**, 125018 (2024).

[84] M. S. Crosser, J. Huang, F. Pierre, P. Virtanen, T. T. Heikkilä, F. K. Wilhelm, and N. O. Birge, Nonequilibrium transport in mesoscopic multi-terminal SNS Josephson junctions, Phys. Rev. B **77**, 014528 (2008).

[85] Y. P. Baryshev, A. Vasil'ev, A. Dmitriyev, M. Y. Kupriyanov, V. Lukichev, I. Y. Luk'yanova, A. Orlikovskiy, and I. Sokolova, Theoretical and experimental study of the Josephson effect in submicron SN-N-NS structures, Lithogr. Microelectron. **8**, 187 (1989).

[86] X. Jehl, P. Payet-Burin, C. Baraduc, R. Calemczuk, and M. Sanquer, Andreev reflection enhanced shot noise in mesoscopic SNS junctions, Phys. Rev. Lett. **83**, 1660 (1999).

[87] V. Gubankov, V. Koshelets, G. Ovsyannikov, and A. Vystavkin, Microwave properties of variable thin-film Josephson bridges, IEEE Trans. Magn. **15**, 284 (1979).

[88] V. Conte, J. Giordano, J. Luzuriaga, J. Zárate, and H. Pastoriza, in *Twenty-First International Symposium on Space Terahertz Technology* (Curran Associates, Inc., NY, USA, 2010), pp. 424–427, https://www.nrao.edu/meetings/isstt/papers/2010/2010424427.pdf.

[89] D. Montemurro, D. S. Golubev, S. Kubatkin, F. Tafuri, T. Bauch, and F. Lombardi, Enhanced Josephson coupling in hybrid nanojunctions, Phys. Rev. B **107**, 094517 (2023).

[90] V. Ruzhickiy, S. Bakurskiy, M. Kupriyanov, N. Klenov, I. Soloviev, V. Stolyarov, and A. Golubov, Contribution of processes in SN electrodes to the transport properties of SN-N-NS Josephson junctions, Nanomaterials **13**, 1873 (2023).

[91] S. Bakurskiy, V. Ruzhickiy, A. Neilo, N. Klenov, I. Soloviev, A. Elistratova, A. Shishkin, V. Stolyarov, and M. Kupriyanov, Thouless energy in Josephson SN-N-NS bridges, Mesosci. Nanotechnol. **1**, 01003 (2024).

[92] D. V. Baxter, S. D. Steenwyk, J. Bass, and W. P. Pratt, Resistance and spin-direction memory loss at Nb/Cu interfaces, J. Appl. Phys. **85**, 4545 (1999).

[93] W. Park, D. V. Baxter, S. Steenwyk, I. Moraru, W. P. Pratt, and J. Bass, Measurement of resistance and spin-memory loss (spin relaxation) at interfaces using sputtered current perpendicular-to-plane exchange-biased spin valves, Phys. Rev. B **62**, 1178 (2000).

[94] A. Sharma, J. A. Romero, N. Theodoropoulou, R. Loloee, W. P. Pratt, Jr., and J. Bass, Specific resistance and scattering asymmetry of Py/Pd, Fe/V, Fe/Nb, and Co/Pt interfaces, J. Appl. Phys. **102**, 113916 (2007).
[95] E. Tuuli and K. Gloos, Normal reflection at superconductor – normal metal interfaces due to Fermi surface mismatch, J. Phys.: Conf. Ser. **400**, 042066 (2012).
[96] J. Bass, CPP magnetoresistance of magnetic multilayers: A critical review, J. Magn. Magn. Mater. **408**, 244 (2016).
[97] V. S. Stolyarov, T. Cren, C. Brun, I. A. Golovchanskiy, O. V. Skryabina, D. I. Kasatonov, M. M. Khapaev, M. Yu. Kupriyanov, A. A. Golubov, and D. Roditchev, Expansion of a superconducting vortex core into a diffusive metal, Nat. Commun. **9**, 2217 (2018).
[98] A. A. Golubov, E. P. Houwman, J. G. Gijsbertsen, V. M. Krasnov, J. Flokstra, H. Rogalla, and M. Yu. Kupriyanov, Proximity effect in superconductor-insulator-superconductor Josephson tunnel-junctions – theory and experiment, Phys. Rev. B **51**, 1073 (1995).
[99] A. Zehnder, Ph. Lerch, S. P. Zhao, Th. Nussbaumer, E. C. Kirk, and H. R. Ott, Proximity effects in Nb/Al-AlO_x-Al/Nb superconducting tunneling junctions, Phys. Rev. B **59**, 8875 (1999).
[100] G. Brammertz, A. Poelaert, A. A. Golubov, P. Verhoeve, A. Peacock, and H. Rogalla, Generalized proximity effect model in superconducting bi- and trilayer films, J. Appl. Phys. **90**, 355 (2001).
[101] A. A. Golubov, E. P. Houwman, J. G. Gijsbertsen, V. M. Krasnov, J. Flokstra, H. Rogalla, and M. Yu. Kupriyanov, Proximity effect in superconductor-insulator-superconductor Josephson tunnel junctions: Theory and experiment, Phys. Rev. B **51**, 1073 (1995).
[102] V. Lacquaniti, S. Gonzini, S. Maggi, E. Monticone, R. Steni, and D. Andreone, New barriers for fast-switching SNS Josephson junctions, Int. J. Mod. Phys. B **13**, 1259 (1999).
[103] V. Lacquaniti, S. Maggi, E. Monticone, A. Polcari, R. Steni, and D. Andreone, Development of a Nb-Al technology for SNS Josephson junctions, Int. J. Mod. Phys. B **14**, 3044 (2000).
[104] V. Lacquaniti, S. Maggi, E. Monticone, A. Polcari, R. Steni, and D. Andreone, High-resistivity superconductor-normal-superconductor junctions for an AC Josephson voltage standard, Philos. Mag. B **80**, 965 (2000).
[105] V. Lacquaniti, S. Maggi, R. Steni, C. Cagliero, R. Rocci, and D. Andreone, Fabrication process of Nb-Al/Nb SNS Josephson junctions for superconducting electronics applications, Int. J. Mod. Phys. B **17**, 696 (2003).
[106] V. Lacquaniti, S. Maggi, R. Steni, C. Cagliero, D. Andreone, and R. Rocci, Nb-Al/Nb junctions with a wide range of characteristic voltages for superconducting electronic applications, IEEE Trans. Appl. Supercond. **13**, 146 (2003).
[107] D. Andreone, C. Cagliero, V. Lacquaniti, S. Maggi, A. Polcari, and R. Steni, Electrical and structural properties of Nb-Al/Nb overdamped Josephson junctions, Physica C **372–376**, 34 (2002).
[108] V. Bosboom, J. J. W. Van der Vegt, M. Yu. Kupriyanov, and A. A. Golubov, Selfconsistent 3D model of SN-N-NS Josephson junctions, Supercond. Sci. Technol. **34**, 115022 (2021).
[109] K. D. Usadel, Generalized diffusion equation for superconducting alloys, Phys. Rev. Lett. **25**, 507 (1970).
[110] M. Y. Kuprianov and V. F. Lukichev, Effect of boundary transparency on critical current in dirty SS'S structures, Zh. Eksp. Teor. Fiz. **94**, 139 (1988). [Sov. Phys. JETP **67**, 1163 (1988)].
[111] N. Cai, G. Zhou, K. Müller, and D. E. Starr, Effect of oxygen gas pressure on the kinetics of alumina film growth during the oxidation of Al(111) at room temperature, Phys. Rev. B **84**, 125445 (2011).
[112] N. Joshi, A. K. Debnath, D. K. Aswal, K. P. Muthe, M. S. Kumar, S. K. Gupta, and J. V. Yakhmi, Morphology and resistivity of Al thin films grown on Si (1 1 1) by molecular beam epitaxy, Vacuum **79**, 178 (2005).
[113] E. Sedov, Issledovanie kriticheskoi temperaturi sverkhprovodyashego perehoda tonkih plenok aluminiya [Study on superconducting transition critical temperature of aluminum thin film] (in Russian), Ph.D. thesis, HSE, 2024.
[114] L. Capogna and M. G. Blamire, Superconducting proximity effect through high-quality high-conductance tunnel barriers, Phys. Rev. B **53**, 5683 (1996).
[115] I. P. Nevirkovets, J. B. Ketterson, and S. Lomatch, Anomalous critical current in double-barrier Nb/Al–AlO_x–Al–AlO_x–Nb devices, Appl. Phys. Lett. **74**, 1624 (1999).
[116] D. Balashov, F.-Im. Buchholz, H. Schulze, M. I. Khabipov, R. Dolata, M. Y. Kupriyanov, and J. Niemeyer, Stationary properties of SINIS double-barrier Josephson junctions, Supercond. Sci. Technol. **13**, 244 (2000).
[117] S. L. Prischepa and V. N. Kushnir, Phonon softening in nanostructured phonon–mediated superconductors, J. Phys.: Condens. Matter **35**, 313003 (2023).
[118] K. Yu. Arutyunov, E. A. Sedov, V. V. Zavialov, A. Stavrinidis, G. Stavrinidis, Z. Chatzopoulos, A. Adikimenakis, G. Konstantinidis, N. Florini, P. Chatzopoulou *et al.*, The critical temperature of superconducting aluminum films, Phys. Met. Metallogr. **124**, 53 (2023).
[119] S. Nik, P. Krantz, L. Zeng, T. Greibe, H. Pettersson, S. Gustafsson, P. Delsing, and E. Olsson, Correlation between Al grain size, grain boundary grooves and local variations in oxide barrier thickness of Al/AlO_x/Al tunnel junctions by transmission electron microscopy, SpringerPlus **5**, 1067 (2016).
[120] A. Fedotov, O. Severyukhina, A. Salomatina, V. Boian, and A. Sidorenko, Numerical study of magnetic properties for Co-Fe-Nb nanofilms as promising materials for magnetoresistive memory, Mesosci. Nanotechnol. **1**, (2025).
[121] Z. Nishiyama, X-ray investigation of the mechanism of the transformation from face-centred cubic lattice to body-centred cubic, Sci. Rep. Tohoku Imp. Univ. **23**, 637 (1934).
[122] G. Wassermann, Über den mechanismus der $\alpha \rightarrow \gamma$ umwandlung des eisens, Mitteilungen aus dem Kaiser–Wilhelm–Institut für Eisenforschung **17**, 149 (1935).
[123] T. F. Coleman and Y. Li, An interior trust region approach for nonlinear minimization subject to bounds, SIAM J. Optim. **6**, 418 (1996).
[124] T. F. Coleman and Y. Li, On the convergence of reflective Newton methods for large-scale nonlinear minimization subject to bounds, Math. Program. **67**, 189 (1994).